metals

MDPI

Article

Comparative Study on the Liquid Metal Embrittlement Susceptibility of the High-Si Advanced High-Strength Steel with EG and GA Zn Coatings

Jingyi Gu [1], Jiayi Zhou [1], Rongxun Hu [1], Yu Sun [1], Ming Lei [2,3,*] and Yulai Gao [1,*]

[1] State Key Laboratory of Advanced Special Steel, School of Materials Science and Engineering, Shanghai University, Shanghai 200444, China; gjy0309@shu.edu.cn (J.G.); zhoujy00@shu.edu.cn (J.Z.); rongxunhu@shu.edu.cn (R.H.); sunyu00@shu.edu.cn (Y.S.)
[2] State Key Laboratory of Development and Application Technology of Automotive Steels (Baosteel Group), Shanghai 201900, China
[3] Automobile Steel Research Institute, R&D Center, Baoshan Iron & Steel Co., Ltd., Shanghai 201900, China
* Correspondence: lei_ming@baosteel.com (M.L.); ylgao@shu.edu.cn (Y.G.)

Abstract: The Zn-coated high-Si advanced high-strength steel (AHSS) tends to suffer Zn-assisted liquid metal embrittlement (LME) during the resistance spot welding (RSW) process. In this study, the LME behaviors of electrogalvanized (EG) and galvannealed (GA) high-Si steels were comparatively investigated. The maximum lengths of the LME cracks at the shoulder and center of the spot weld were approximately 366.6 μm and 1486.5 μm, respectively, for the EG yet 137.0 μm and 1533.3 μm, respectively, for the GA high-Si steels. Additionally, all EG and GA welded joints were etched to measure the nugget size. It was found that the increased welding current could aggravate the formation tendency of the LME cracks for both the EG and GA high-Si steels. Furthermore, the statistical results revealed that the electrogalvanized high-Si AHSS exhibited a relatively higher LME susceptibility than the galvannealed high-Si AHSS. It was deemed that the internal oxidation produced during the annealing before the Zn coating was the crucial factor that led to the difference in the LME susceptibilities for the EG and GA high-Si steels.

Keywords: LME susceptibility; electrogalvanized steel; galvannealed steel; high Si content; resistance spot welding

check for updates

Citation: Gu, J.; Zhou, J.; Hu, R.; Sun, Y.; Lei, M.; Gao, Y. Comparative Study on the Liquid Metal Embrittlement Susceptibility of the High-Si Advanced High-Strength Steel with EG and GA Zn Coatings. *Metals* **2024**, *14*, 1221. https://doi.org/10.3390/met14111221

Academic Editor: Frank Czerwinski

Received: 18 September 2024
Revised: 18 October 2024
Accepted: 24 October 2024
Published: 26 October 2024

Copyright: © 2024 by the authors. Licensee MDPI, Basel, Switzerland. This article is an open access article distributed under the terms and conditions of the Creative Commons Attribution (CC BY) license (https://creativecommons.org/licenses/by/4.0/).

1. Introduction

Advanced high-strength steels (AHSSs) are developed with a good combination of strength and formability to realize light weight in automobile manufacturing and production, which contributes to emission reduction, energy conservation, and crash safety [1–4]. The high-Si AHSS is heat-treated by the quenching and partitioning process with the microstructure of a mixture of the ferrite, martensite, and retained austenite at room temperature, which is distinguished by excellent strength, formability, and economy efficiency [5–7].

Zn coatings are extensively used to protect the steel substrate [8]. Zn-based coatings are categorized into three common types involving hot dip galvanized (GI), electrogalvanized (EG), and galvannealed (GA) coatings [9]. GI is the mainly used method attributing to its simple manufacturing process, low cost, and excellent weldability conditions [10]. The GI process is to dip the steel plate in a Zn bath (~460 °C), where Zn and steel react to form a Zn coating on the surface of the steel [11]. EG is the electrodeposition of the Zn coating on the steel surface [12]. The EG coating is denser, thinner, and more uniform than the GI coating and reveals better corrosion resistance [13]. The GA process includes the GI process and a subsequent alloying process via a heat treatment after hot dipping [14]. Fe from the steel substrate and Zn from the GA coating react to form various Fe-Zn intermetallic phases [15].

The GA coating is acquiring increasingly more markets attributing to its lower cost and more excellent weldability conditions than the EG coating [16].

Resistance spot welding (RSW), as the leading technique of metal joining in the automotive industry, is predominantly applied to join the AHSS sheets during vehicle assembly [17]. Unfortunately, Zn-assisted liquid metal embrittlement (LME) tends to occur in the Zn-coated high-Si AHSS during the RSW process due to the presence of molten Zn [18]. Zn melts at about 420 °C, far below the melting point of the steel substrate (~ 1500 °C) [19]. When the temperature reaches significantly higher than the melting point of Zn during the RSW process, liquid Zn can penetrate into the steel substrate under large tensile stress, leading to the weakening of the solid metal grain boundaries and intergranular fracture [20,21]. The LME phenomenon catastrophically deteriorates the mechanical properties of Zn-coated high-Si steels [22]. Various factors can produce the influences on the formation of the LME, including the substrate microstructure, chemical composition, and welding parameters [23–25]. Bhattacharya et al. [26] found that the dual phase (DP) steel exhibited a lower LME susceptibility than the transformation-induced-plasticity (TRIP)-assisted bainitic ferrite (TBF), quenched and partitioned (QP) or martensitic steels, attributing to the presence of discrete martensite islands, ultrafine ferrite grains, and a smaller area fraction of prior austenite grain boundaries in the DP microstructure. Akbari et al. [27] discovered that the addition of element B which led to lower grain boundary energy could prevent the Mn segregation, eventually reducing Zn-assisted LME susceptibility. Wintjes et al. [28] noticed that multiple pulse welding schedules could be applied to reduce the LME severity successfully.

In particular, the choice of galvanizing technique is also a crucial factor for the formation of LME during the RSW process, because the microstructure varies with different processing histories [29]. DiGiovanni et al. [30] reported that the Zn-coated TRIP steel displayed a more severe LME cracking which significantly decreased the lap shear strength of TRIP steel compared with the uncoated TRIP steel. Tolf et al. [31] observed that by using the same welding parameters and base material, the first 50 spot welds with EG coating were all free of cracks, while only 10 out of 50 spot welds with GI coating were crack-free for the DP steel. Ashiri et al. [29] detected that electrogalvanized twinning-induced plasticity (TWIP) steel exhibited a lower LME susceptibility than galvanized and galvannealed TWIP steels based on the critical nugget diameter. El-Sari et al. [32] found that EG was identified as the most LME-resistant coating for the DP steel compared to GI and GA based on occurrence rate and crack length. However, the above-mentioned studies only comparatively investigated the impact of different Zn coatings on the LME susceptibility. The high-Si advanced high-strength steel is a typical system among the third-generation AHSSs. The LME susceptibility of this high-Si advanced high-strength steel with EG and GA Zn coatings has not been fully evaluated, which in fact limits their application in the automotive industry. It is well known that the evaluation of the LME susceptibility for the Zn-coated steels is the precondition for their application in the automotive industry. Also, the different influences of EG and GA coatings on the LME susceptibility of the high-Si AHSS had not been comparatively studied, and further investigation was still necessary.

In the present study, the LME behaviors of electrogalvanized and galvannealed high-Si steels were comparatively researched by changing the welding current during the RSW process. The crack characteristics of the electrogalvanized and galvannealed high-Si steels under various welding currents were investigated, including the maximum crack length, crack amount, and nugget size. Furthermore, the difference in the LME susceptibilities for electrogalvanized and galvannealed high-Si steels was comprehensively analyzed, and the correlation between the LME susceptibility and the Zn coating was correspondingly discussed.

2. Materials and Methods

The materials used in this study were EG and GA high-Si steels with a thickness of 1.4 mm. The chemical composition of the high-Si steels is listed in Table 1. The EG and GA

high-Si steels exhibited similar mechanical properties evaluated via the tensile shear test on the electronic universal testing machine (Instron 5581, Instron, Norwood, MA, USA), as displayed in Table 2. For the specimen of the tensile shear welded joint, the EG and GA high-Si advanced high-strength steel sheets were cut to a length of 285 mm, width of 25 mm, and overlap length of 130 mm, as shown in Figure 1. The equal thickness plates with the same thickness of 1.4 mm and length of 150 mm were welded to reduce possible sheet bending and nugget rotation during the tensile shear test. The diameter of welded joints was ~10 mm.

Table 1. Chemical composition of the as-prepared high-Si advanced high-strength steels (wt. %).

Elements	C	Mn	Si	P	S
Nominal composition	>0.20	>1.8	>1.6	<0.030	<0.010
Practical composition	0.21	2.0	1.8	0.012	0.001

Table 2. Mechanical properties of the as-prepared electrogalvanized (EG) and galvannealed (GA) high-Si advanced high-strength steels.

Mechanical Properties	Tensile Strength (MPa)	Yield Strength (MPa)	Elongation (%)
EG specimen	1049	641	21.5
GA specimen	1018	703	22.5

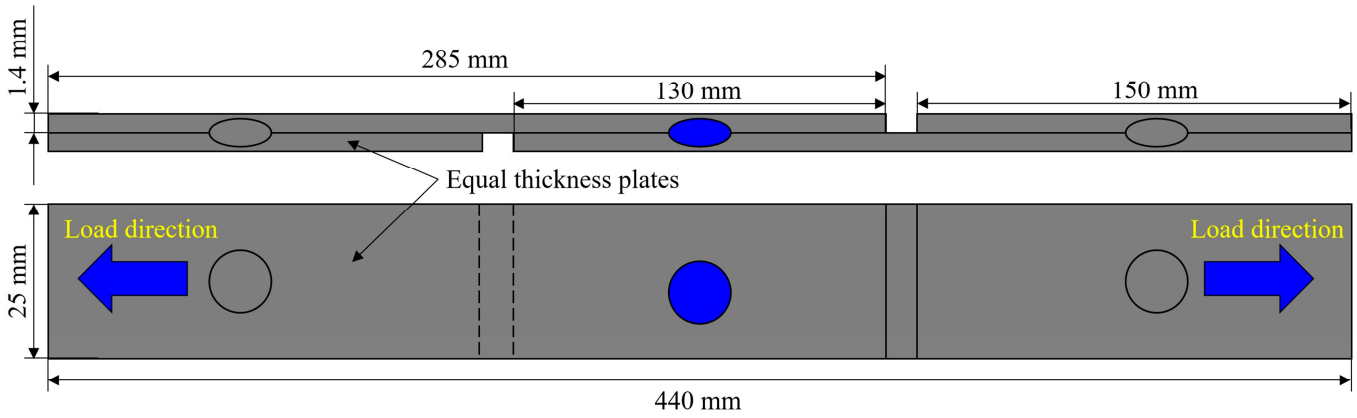


Figure 1. Schematic of the dimensions of the RSW joint of the tensile–shear specimen.

The test method applied in this study was the rapid liquid metal embrittlement test procedure (ASP LP#3.1, Auto/Steel Partnership, Ann Arbor, MI, USA) for coated sheet steel according to the requirements of the Auto/Steel Partnership (A/SP) criterion [33]. The EG and GA specimens were welded at 16 groups of different pulse currents. The squeeze time was 1000 ms. The current profile was 8 progressive sloping impulses with a heating duration of 130 ms and a cooling duration of 40 ms. The first impulse began at 5.0 kA, and the last impulse ended at a designated final amperage ranging from 7.0 to 14.5 kA, with intervals of 0.5 kA. The hold time was 250 ms. The electrode force was 4.0 kN. The employed Cu-Zr electrode cap was type F1 based on the standard "International Organization for Standardization (ISO) 5821" [34]. The engineering stress–strain curve of the welded joint fabricated without any defects was presented in Figure 2. Also, the corresponding mechanical properties of the welded joint fabricated without any defects were listed in Table 3.

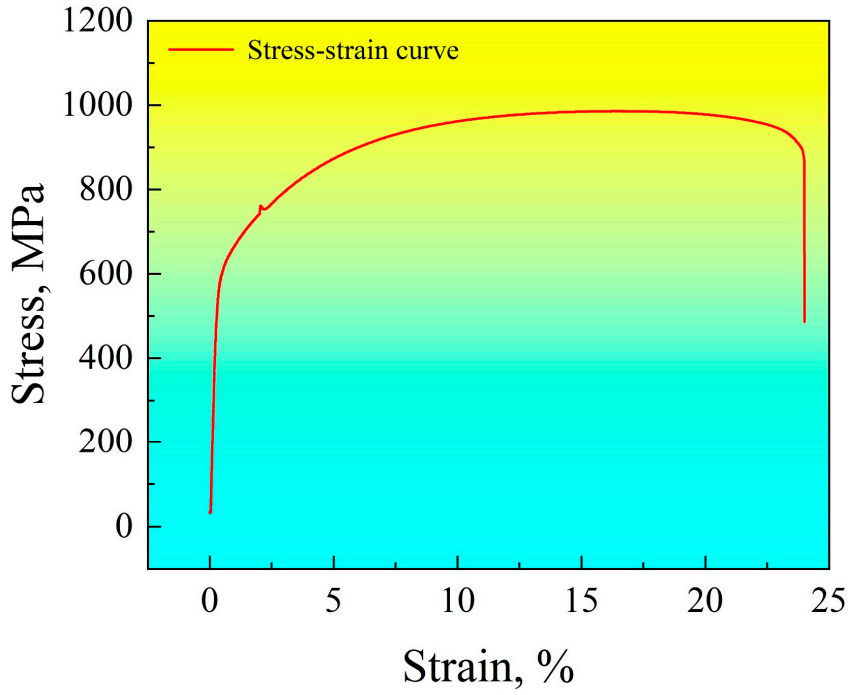


Figure 2. The engineering stress–strain curve of the welded joint fabricated without any defects.

Table 3. Mechanical properties of the welded joint fabricated without any defects.

Mechanical Properties	Tensile Strength (MPa)	Yield Strength (MPa)	Elongation (%)
Welded joint fabricated without any defects	986	600	16.3

The evaluation of the LME susceptibility of the Zn-coated AHSSs was based on the A/SP criterion [33]. The LME cracks are divided into four types. The surface cracks inside the electrode imprint (center of the spot weld) were defined as type A. Type B cracks could be observed outside the electrode imprint. The interfacial surface cracks were categorized as type C. Type D cracks appeared in the outer transition imprint (shoulder of the spot weld).

To reveal the existence of surface cracks, the Zn coating on the surface of the welded joint was firstly removed by pickling in a $(CH_2)_6N_4$-HCl solution with a dipping time of 30 s. The surface cracks of the welded joint were observed by the automated digital microscope (Zeiss Smartzoom 5, Zeiss, Oberkochen, Germany). Then, the RSW joint in each group was cut, ground, and polished perpendicular to the longest surface crack. To display the nugget size of the welded joint, the cross section of the RSW joint in each group was etched in a 4 vol.% nital solution. The crack lengths, location, and nugget size in the cross section were observed by the optical microscope (OM, Zeiss Axio Imager A2m, Zeiss, Oberkochen, Germany).

3. Results and Discussion

3.1. Surface Morphology of the RSW Joints at Various Welding Currents

To study and compare the LME behaviors of electrogalvanized and galvannealed high-Si steels, the surface morphology and microstructure in the cross sections of the LME cracks of 16 groups of electrogalvanized and galvannealed welded joints with different welding currents were observed, among which four typical groups of electrogalvanized and galvannealed welded joints at 8.5 kA, 10.5 kA, 12.5 kA, and 14.5 kA were emphasized. Figure 3 shows the surface morphology of those four typical groups of EG and GA welded

joints. For both EG and GA welded joints, no obvious surface cracks could be observed at 8.5 kA, as displayed in Figure 3a,e. On the contrary, some short surface cracks appeared at 10.5 kA (see Figure 3b,f). Figure 3c,g revealed that many long surface cracks were formed when the welding current was increased to 12.5 kA. Eventually, more severe surface cracks could be clearly observed at 14.5 kA, as shown in Figure 3d,h.

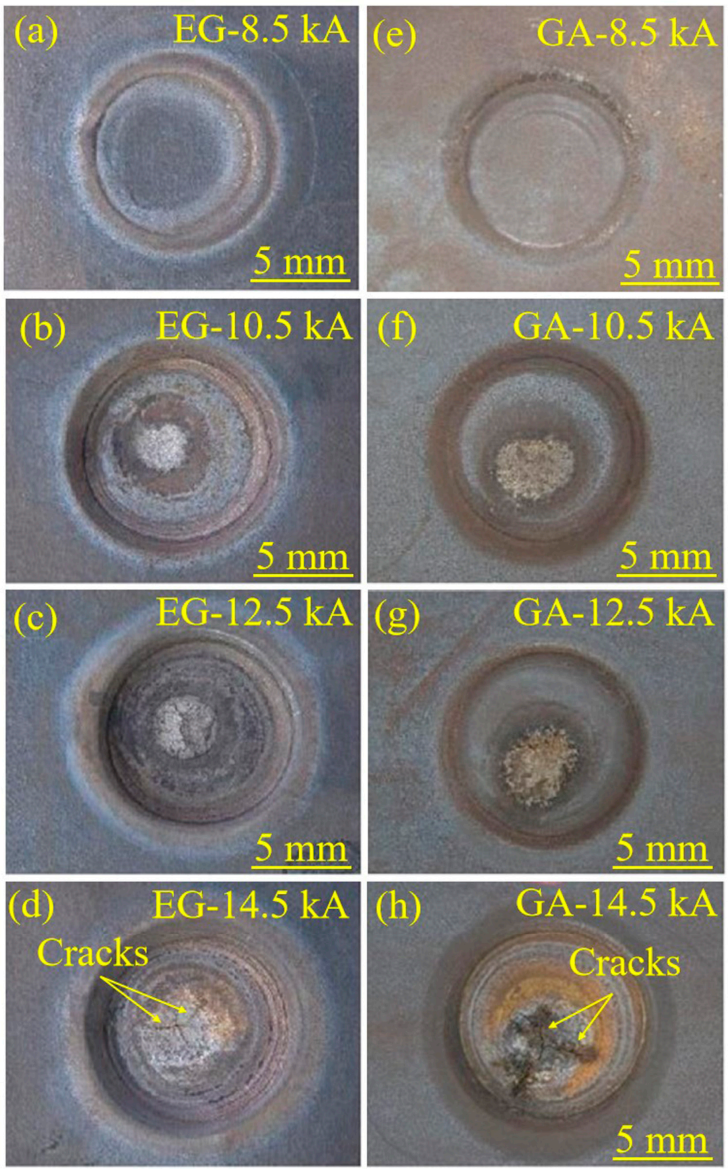


Figure 3. Surface morphology after pickling of the RSW specimens: (**a**–**d**) the electrogalvanized (EG) welded joints at welding currents of 8.5 kA, 10.5 kA, 12.5 kA, and 14.5 kA, respectively, and (**e**–**h**) the galvannealed (GA) welded joints at welding currents of 8.5 kA, 10.5 kA, 12.5 kA, and 14.5 kA, respectively.

3.2. LME Crack Characterization at Different Welding Currents

The cross sections of those above-mentioned four typical groups of electrogalvanized and galvannealed welded joints perpendicular to the longest surface cracks without chemical etching were displayed to further investigate the existence characteristics of the LME cracks at various welding currents for the high-Si AHSS with EG and GA Zn coatings during the RSW process. Figure 4 presents that no LME cracks could be observed for both EG and GA welded joints at 8.5 kA. However, expulsion started at 10.5 kA and 10.0 kA for the EG and GA specimens, respectively. When the welding current was increased to

10.5 kA, the LME cracks of type A and D appeared. The maximum lengths of type A and D cracks were approximately 73.2 μm and 130.5 μm, respectively, for the EG yet 197.1μm and 124.0 μm, respectively, for the GA welded joint, as shown in Figure 5. With increasing the welding current, the high temperature could reduce the surface tension of liquid metal and accelerate the mobility of the liquid Zn atoms [35]. On the other hand, the large tensile stress caused by the deep indentation could expand the grain boundaries, which extended the path for the Zn penetration and thus led to the LME cracks [36].

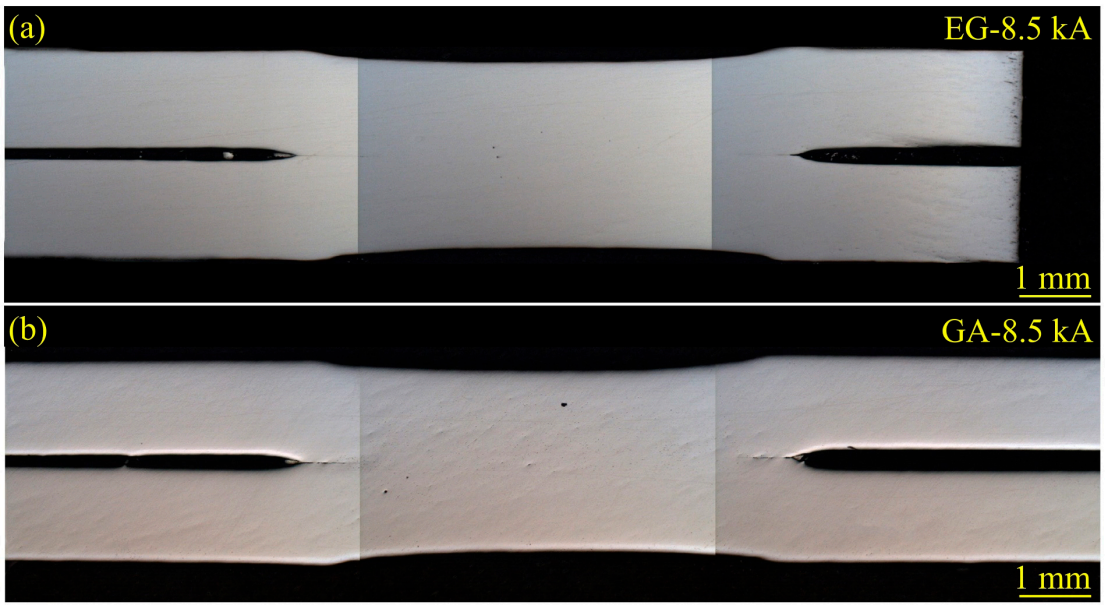


Figure 4. Metallographical images of the LME cracks in the cross sections of the specimens at a welding current of 8.5 kA: (**a**) the overall macrostructure of the electrogalvanized (EG) welded joint and (**b**) the overall macrostructure of the galvannealed (GA) welded joint.

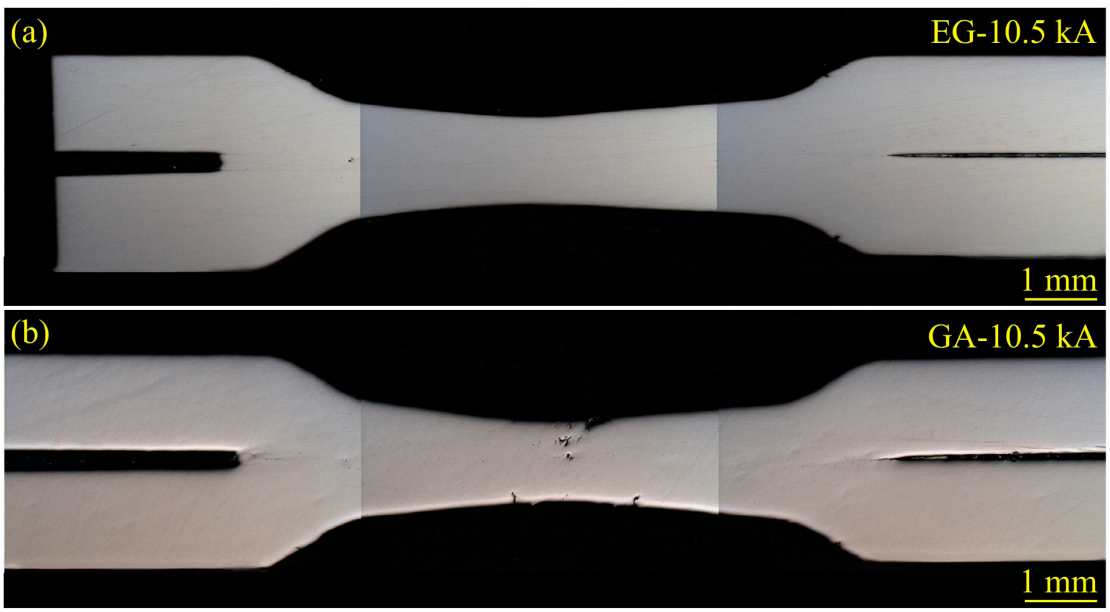


Figure 5. Metallographical images of the LME cracks in the cross sections of the specimens at a welding current of 10.5 kA: (**a**) the overall macrostructure of the electrogalvanized (EG) welded joint and (**b**) the overall macrostructure of the galvannealed (GA) welded joint.

Figure 6 depicts the cross sections of the EG and GA welded joints at 12.5 kA, and plenty of long LME cracks can be clearly observed. The longest type A crack for the EG welded joint was measured as around 1222.1 μm, while the maximum crack length of type A for the GA welded joint was about 1053.3 μm. There also existed many type D cracks, with the longest crack measured as approximately 194.8 μm for the EG yet 111.5 μm for the GA welded joint. Eventually, more severe LME cracks were formed when the welding current was increased to 14.5 kA, as displayed in Figure 7. The longest LME cracks of type A and D for the EG welded joint were around 563.8 μm and 129.1 μm, respectively. In contrast, the maximum LME crack lengths of type A and D for the GA welded joint were approximately 1387.5 μm and 98.6 μm, respectively. In comparison with the EG and GA welded joints presented in Figures 4–6, it was found that the increase in the welding current led to more and longer LME cracks for both EG and GA specimens. Generally, the LME cracks were formed via the intergranular propagation mode in the steel [37]. Increasing the welding current generated high heat input and large tensile stress, leading to brittle intergranular fracture during the RSW process [38]. The Zn coating melted at high temperatures, then the liquid Zn could penetrate into the grain boundaries under the large tensile stress which exceeded the yield stress of the steel at some specific temperature range, triggering the formation of the LME cracks [9]. Moreover, Ikeda et al. [39] provided evidence that intermetallic phase formation appeared before the cracking and subsequent penetration of the liquid Zn, and the secondary phase nucleation and growth of Fe-Zn intermetallic compounds (IMCs) led to the LME cracking of Zn-coated advanced high-strength steel. In our previous study, the brittle Γ-Fe_3Zn_{10} IMCs were found to be formed at the grain boundaries in the Zn-coated high-Si steel during the RSW process, which could weaken the cohesion of the grain boundaries, resulting in the propagation of the LME cracks [40]. With the increased welding current, the sufficient spot-welding heat aggravated the formation of Zn-Fe IMCs, which provided the paths for the penetration of liquid Zn [41]. Therefore, increasing the welding current could aggravate the formation tendency of the LME cracks for both electrogalvanized and galvannealed high-Si steels. Moreover, the maximum lengths of type D cracks for the EG welded joints were much larger than those for the GA welded joints at every welding current based on those four above-mentioned typical groups of EG and GA welded joints.

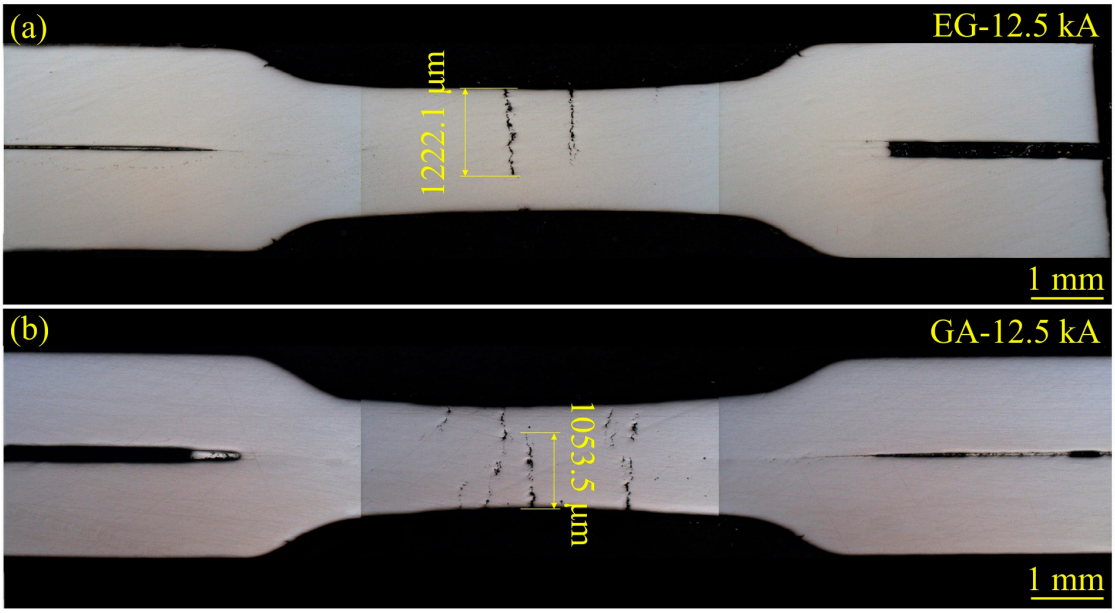


Figure 6. Metallographical images of the LME cracks in the cross sections of the specimens at a welding current of 12.5 kA: (**a**) the overall macrostructure of the electrogalvanized (EG) welded joint and (**b**) the overall macrostructure of the galvannealed (GA) welded joint.

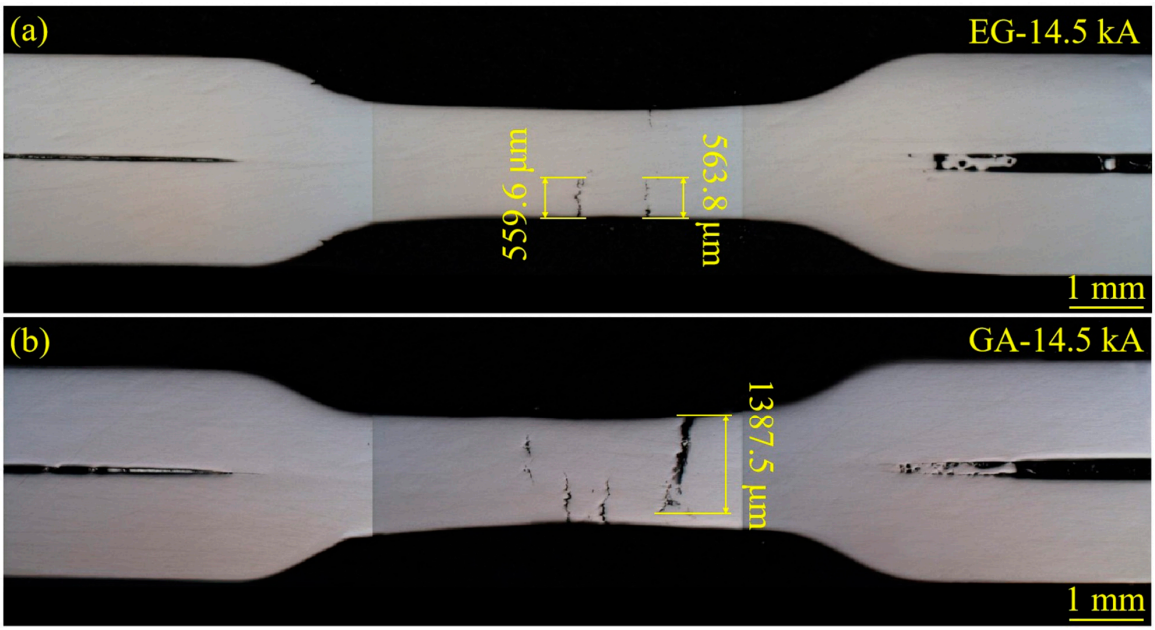


Figure 7. Metallographical images of the LME cracks in the cross sections of the specimens at a welding current of 14.5 kA: (**a**) the overall macrostructure of the electrogalvanized (EG) welded joint and (**b**) the overall macrostructure of the galvannealed (GA) welded joint.

In particular, the longest type D cracks for EG and GA specimens welded at different currents are shown in Figures 8 and 9, respectively. The longest type D crack for the EG specimen was approximately 366.6 μm observed at 10.0 kA, while the longest type D crack for the GA specimen was around 137.0 μm observed at 11.0 kA, as presented in Figures 8b and 9b. In addition, for the EG specimen, the LME cracks of type B only appeared at 10.0 kA with the maximum length measured as approximately 91.9 μm (see Figure 8c), yet no type B LME cracks could be observed in the GA specimen.

To further explore the correlation between the nugget size and welding current, the cross sections of electrogalvanized and galvannealed welded joints welded at 16 groups of different welding currents were all chemically etched. Those above-mentioned four typical groups of electrogalvanized and galvannealed welded joints were emphasized, as revealed in Figure 10. The nugget sizes of EG welded joints were 4909.0 μm, 6103.2 μm, 6340.9 μm, and 6009.7 μm at welding currents of 8.5 kA, 10.5 kA, 12.5 kA, and 14.5 kA, respectively. In contrast, the nugget sizes were 4951.3 μm, 5358.8 μm, 5070.3 μm, and 5702.8 μm for the GA welded joints at 8.5 kA, 10.5 kA, 12.5 kA, and 14.5 kA, respectively. It was found that the nugget size increased with increasing the welding current. Ashiri et al. [29] discovered that the LME cracks were formed when the maximum nugget size at expulsion was larger than the critical nugget size of LME. Lalachan et al. [42] reported that when the nugget growth exceeded the growth of electrode–sheet contact, severe LME cracks were formed. It was considered that the nugget growth was closely related to the formation tendency of the LME cracks. The further nugget growth indicated that the molten metal in the nugget was increased via the heat input generated by increasing the welding current, therefore aggravating the tendency of expulsion during the RSW process [42]. Expulsion could deepen the electrode indentation, which led to larger tensile stress and resultantly caused the LME cracks [29]. Consequently, the further nugget growth could aggravate the formation tendency of the LME cracks. Furthermore, the largest nugget size was 6679.5 μm observed at 13.5 kA for the EG specimen yet 6021.2 μm observed at 9.5 kA for the GA specimen, reflecting the higher LME susceptibility of the EG specimens than the GA ones.

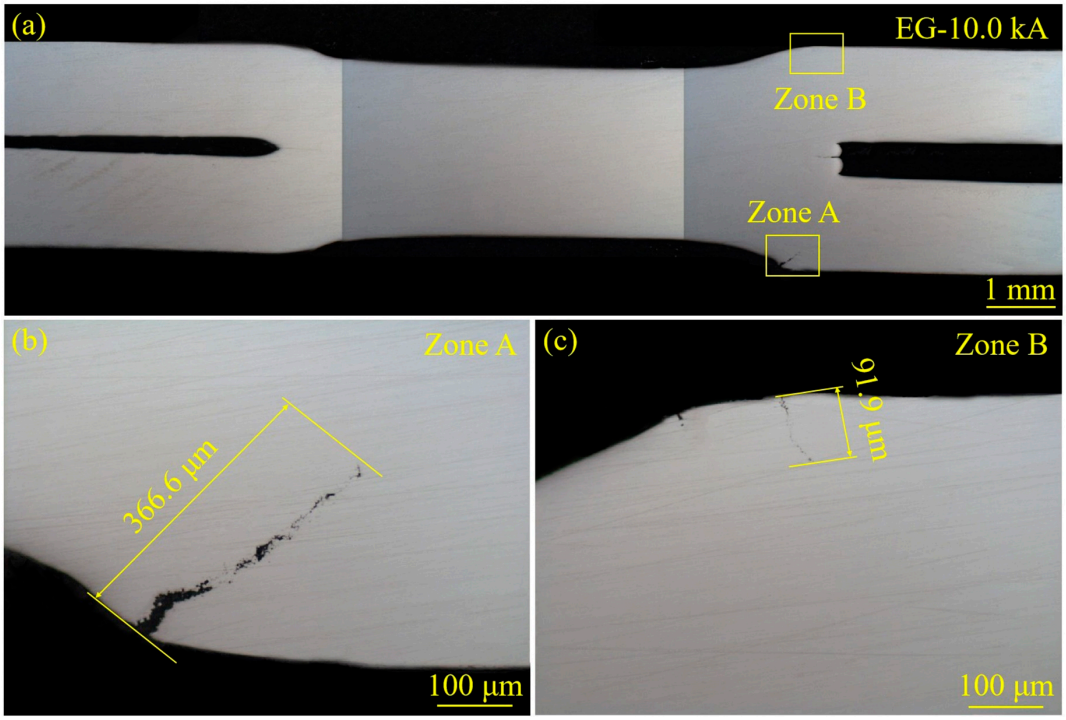


Figure 8. Metallographic images of the LME cracks in the cross section of electrogalvanized (EG) welded joint at a welding current of 10.0 kA: (**a**) the overall macrostructure of the welded joint, (**b**) microstructure of the type D crack in Zone A indicated by the yellow rectangle in (**a**), and (**c**) microstructure of the type B crack in Zone B indicated by the yellow rectangle in (**a**).

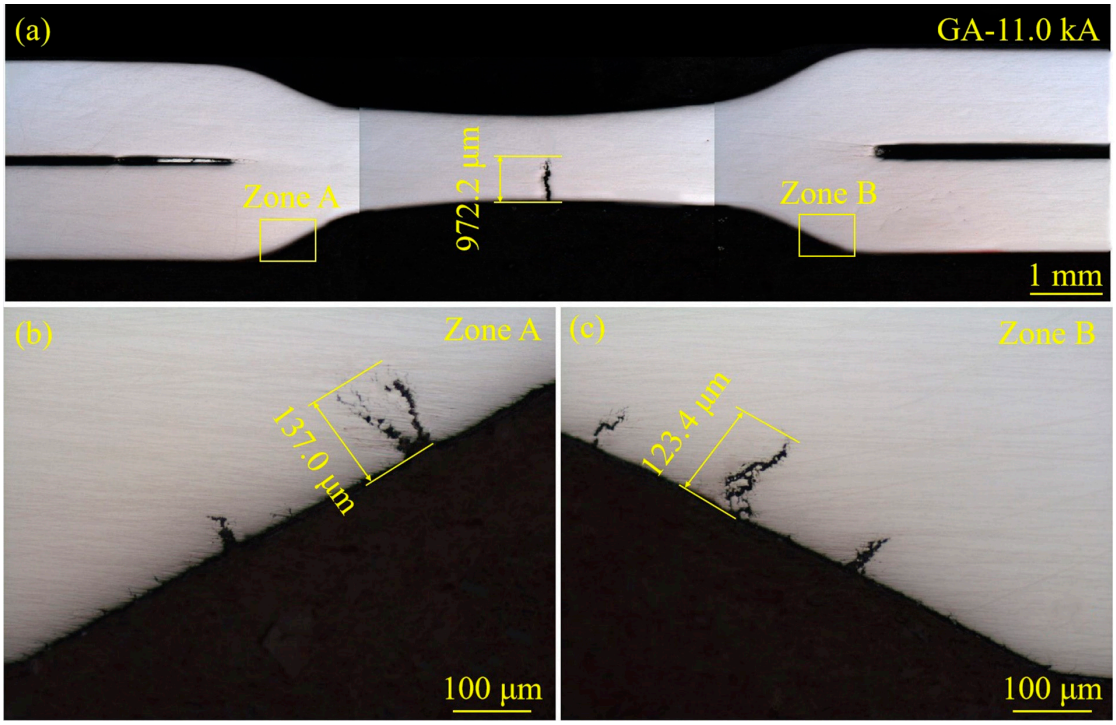


Figure 9. Metallographic images of the LME cracks in the cross section of galvannealed (GA) welded joint at a welding current of 11.0 kA: (**a**) the overall macrostructure of the welded joint, (**b**) microstructure of the type D crack in Zone A indicated by the yellow rectangle in (**a**), and (**c**) microstructure of the type D crack in Zone B indicated by the yellow rectangle in (**a**).

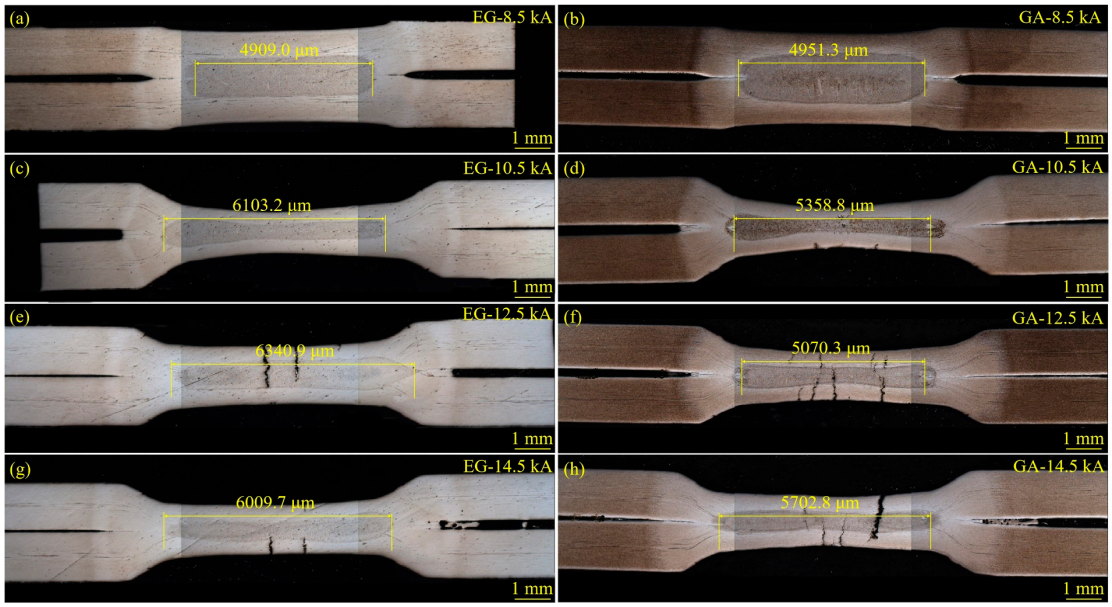


Figure 10. Metallographical images of the nugget sizes in the cross sections of the specimens with chemical etching: (**a**), (**c**), (**e**), and (**g**) show the electrogalvanized (EG) welded joints at welding currents of 8.5 kA, 10.5 kA, 12.5 kA, and 14.5 kA, respectively, and (**b**), (**d**), (**f**), and (**h**) show the galvannealed (GA) welded joints at welding currents of 8.5 kA, 10.5 kA, 12.5 kA, and 14.5 kA, respectively.

3.3. Difference of the LME Susceptibilities for the EG and GA High-Si Advanced High-Strength Steels

To evaluate and compare the LME susceptibilities of electrogalvanized and galvannealed high-Si steels, the amount and maximum lengths of the LME cracks in the cross sections of electrogalvanized and galvannealed welded joints welded at 16 groups of different welding currents were counted and measured, respectively, as exhibited in Figure 11. The LME cracks in both EG and GA specimens began to appear at 10.0 kA. For the EG specimen, the longest LME crack of type A was around 1486.5 μm observed at 14.0 kA, and the maximum length of type D crack was measured as approximately 366.6 μm observed at 10.0 kA. The type B cracks could only be observed at 10.0 kA with a maximum length of about 93.3 μm. For the GA specimen, the maximum crack lengths of type A and D were around 1533.3 and 137.0 μm observed at 13.5 and 11.0 kA, respectively, while no type B LME cracks could be observed. There were no LME cracks of type C observed in both EG and GA specimens. Based on the A/SP criterion, the maximum length of the LME crack more than 5% of the steel thickness for types B, C, and D and 10% for type A was unacceptable below expulsion, while the maximum crack length more than 5% for types B and C and 10% for type D was unacceptable, and there was no need to take type A cracks into consideration at or above expulsion. As for the EG high-Si AHSS, the welded joints at welding currents of 10.0 kA, 12.5 kA, 13.0 kA, and 14.0 kA were not acceptable, as illustrated in Figure 11c. It was found that the electrogalvanized high-Si advanced high-strength steel exhibited high LME susceptibility. In contrast, the galvannealed high-Si advanced high-strength steel completely met the requirements of the A/SP criterion, as shown in Figure 11d, displaying low LME susceptibility. Therefore, it was concluded that the electrogalvanized high-Si advanced high-strength steel exhibited a relatively higher LME susceptibility than that of the galvannealed one, so the application of electrogalvanized high-Si advanced high-strength steel should be controlled in the industrial production.

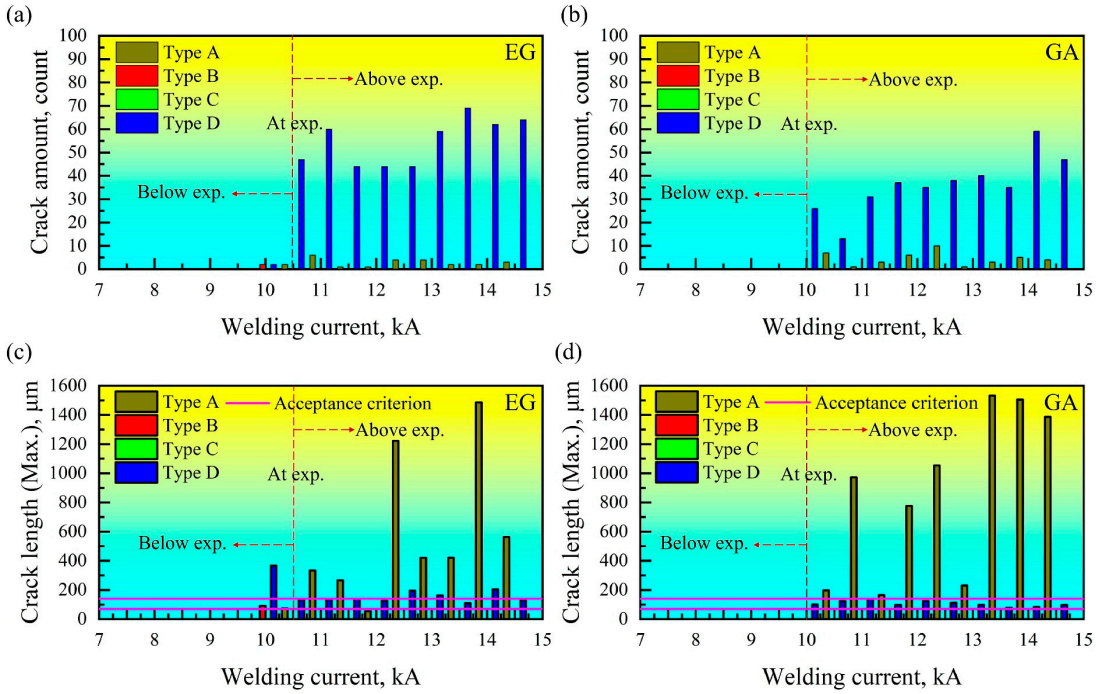


Figure 11. Statistical results of the amount and maximum lengths of the LME cracks for four types at 16 groups of different welding currents and acceptance criterion: the amount of the LME cracks in (**a**) the EG welded joints and (**b**) the GA welded joints; the maximum lengths of the LME cracks in (**c**) the EG welded joints and (**d**) the GA welded joints.

It was deemed that the internal oxidation produced during the annealing before the Zn coating was the crucial factor that led to the difference in the LME susceptibilities for the EG and GA high-Si steels. Generally, during the manufacturing process of Zn-coated AHSS, the annealing process under a controlled atmosphere with a relatively high oxygen partial pressure was applied to promote reactive wetting for the subsequent galvanizing process, and the dew point of the annealing atmosphere varied because of the different galvanizing processes [43]. The internal oxidation layer could be formed between the Zn coating and steel substrate by increasing the dew point during annealing [44]. In our previous study, the internal oxidation layer was found to mitigate the penetration motivation of the liquid Zn, thereby reducing the formation of the LME cracks [45], yet the internal oxidation layer was not observed in the electrogalvanized advanced high-strength steel [46]. Miyata et al. [47] discovered that a high Si/Mn ratio (Si/Mn $\approx$ 1.0) in the galvannealed steel contributed to the formation of SiO_2 internal oxides. Therefore, the SiO_2 internal oxides tended to be formed in the investigated GA advanced high-strength steel with high Si content (Si/Mn $\approx$ 0.9, see Table 1). The internal oxides formed at the grain boundaries had poor wettability with the liquid Zn, which could reduce the motivation for the liquid Zn penetration, inhibiting the formation of LME cracks [45]. It was anticipated that the existence of the internal oxidation layer in the galvannealed high-Si advanced high-strength steel could account for its lower susceptibility in contrast to the electrogalvanized high-Si advanced high-strength steel without the internal oxides.

4. Conclusions

The LME behaviors of EG and GA high-Si steels were comparatively investigated in this study. The crack characteristics of EG and GA high-Si steels under various welding currents were investigated, including the maximum crack length, crack amount, and nugget size. Moreover, the difference in the LME susceptibilities for EG and GA high-Si steels was comprehensively analyzed. Also, the correlation between the Zn coating and the LME susceptibility was correspondingly discussed. The main conclusions are drawn as follows:

(1) The increase in the welding current could lead to more and longer LME cracks, thus aggravating the formation tendency of the LME cracks for both electrogalvanized and galvannealed high-Si steels. The maximum lengths of type A and D cracks were approximately 1486.5 μm and 366.6 μm, respectively, for the EG yet 1533.3 μm and 137.0 μm, respectively, for the GA high-Si steel.

(2) The nugget size increased with increasing the welding current. The further nugget growth indicated that the molten metal in the nugget was increased, which aggravated the tendency of expulsion during the RSW process. Expulsion resulted in deepened electrode indentation and therefore generated larger tensile stress, thereby aggravating the formation tendency of the LME cracks for both EG and GA high-Si steels. Moreover, the largest nugget size for the EG high-Si steel was 6679.5 μm yet 6021.2 μm for the GA high-Si steel, reflecting the higher LME susceptibility of the EG specimens than the GA ones.

(3) The electrogalvanized high-Si advanced high-strength steel exhibited a relatively higher LME susceptibility than that of the galvannealed high-Si advanced high-strength steel. The internal oxidation produced during the annealing before the Zn coating was the crucial factor that led to the difference in the LME susceptibilities for the EG and GA high-Si steels. The existence of the internal oxidation layer in the galvannealed high-Si advanced high-strength steel accounted for its lower susceptibility than the electrogalvanized high-Si advanced high-strength steel without the internal oxidation layer.

Author Contributions: Resources, M.L. and Y.G.; Validation, Y.S.; Formal analysis, J.G., J.Z., R.H., Y.S., and M.L.; Investigation, J.G. and J.Z.; Writing—original draft, J.G.; Writing—review and editing, J.Z., R.H., and Y.G.; Supervision, Y.G. All authors have read and agreed to the published version of the manuscript.

Funding: This research received no external funding.

Institutional Review Board Statement: Not applicable.

Informed Consent Statement: Not applicable.

Data Availability Statement: The original contributions presented in the study are included in the article, further inquiries can be directed to the corresponding authors.

Conflicts of Interest: The authors declare no conflicts of interest. Author Ming Lei is employed by the company Baoshan Iron & Steel Co., Ltd. The remaining authors declare that the research was conducted in the absence of any commercial or financial relationships that could be construed as a potential conflict of interest.

References

1. Galan, J.; Samek, L.; Verleysen, P.; Verbeken, K.; Houbaert, Y. Advanced high strength steels for automotive industry. *Revmetal* **2012**, *48*, 118–131. [CrossRef]
2. Nanda, T.; Singh, V.; Singh, V.; Chakraborty, A.; Sharma, S. Third generation of advanced high-strength steels: Processing routes and properties. *Proc. Inst. Mech. Eng. Pt. L-J. Mater.-Design Appl.* **2019**, *233*, 209–238. [CrossRef]
3. Senuma, T. Processing and properties of advanced high strength steel sheets. *Can. Metall. Q.* **2004**, *43*, 1–12. [CrossRef]
4. Xu, T.; Wu, H.; Xue, F.; Guo, J.; Ran, J.; Gong, F. Structural design of stamping die of advanced high-strength steel part for automobile based on topology optimization with variable density method. *Int. J. Adv. Manuf. Technol.* **2022**, *121*, 8115–8125. [CrossRef]
5. Dong, W.; Ding, K.; Pan, H.; Lei, M.; Gao, Y. Effect of welding current on liquid metal embrittlement of the resistance spot welded galvanized QP980 advanced high-strength steel. In *TMS 2022 151st Annual Meeting & Exhibition Supplemental Proceedings, Anaheim, USA, 27 Feb–03 Mar 2022*; Springer: Cham, Switzerland, 2022; pp. 1254–1261.
6. Li, W.; Ma, L.; Peng, P.; Jia, Q.; Wan, Z.; Zhu, Y.; Guo, W. Microstructural evolution and deformation behavior of fiber laser welded QP980 steel joint. *Mater. Sci. Eng. A-Struct. Mater. Prop. Microstruct. Process.* **2018**, *717*, 124–133. [CrossRef]
7. Wang, S.; Wang, Y.; Yu, L.; Ji, K.; Liu, X.; Lou, Y. Failure modeling for QP980 steel by a shear ductile fracture criterion. *Metals* **2022**, *12*, 452. [CrossRef]
8. Chakraborty, A.; Ghosh, R.; Sudan, M.; Mondal, A. Improvement in hot dip galvanized coating microstructure and properties by pre-metallic deposition on steel surface: A comprehensive review. *Surf. Coat. Technol.* **2022**, *449*, 128972. [CrossRef]
9. Bhattacharya, D. Liquid metal embrittlement during resistance spot welding of Zn-coated high-strength steels. *Mater. Sci. Technol.* **2018**, *34*, 1809–1829. [CrossRef]

10. Zhang, K.; Song, R.; Gao, Y. Corrosion behavior of hot-dip galvanized advanced high strength steel sheet in a simulated marine atmospheric environment. *Int. J. Electrochem. Sci.* **2019**, *14*, 1488–1499. [CrossRef]
11. Smak, M.; Kubicek, J.; Kala, J.; Podany, K.; Vanerek, J. The influence of hot-dip galvanizing on the mechanical properties of high-strength steels. *Materials* **2021**, *14*, 5219. [CrossRef]
12. Lindsay, J.H.; O'Keefe, T.J. Electrogalvanizing. In *Modern Aspects of Electrochemistry*; Conway, B.E., Bockris, R.E.W., Eds.; Springer: New York, NY, USA, 1994; Volume 26, pp. 165–228.
13. Feng, Y.; Li, Y.; Luo, Z.; Ling, Z.; Wang, Z. Resistance spot welding of Mg to electro-galvanized steel with hot-dip galvanized steel interlayer. *J. Mater. Process. Technol.* **2016**, *236*, 114–122. [CrossRef]
14. Chen, L.; Shin, K.S.; Maeng, H.S.; Kang, C.K. Mechanical properties and microstructures development of quenching and partitioning (Q&P) steels during galvannealing process. In *TMS 2023 152nd Annual Meeting & Exhibition Supplemental Proceedings*; Springer: Cham, Switzerland, 2023; pp. 1078–1089.
15. Fang, F.; Du, X.F.; Chen, Y.M. Galvanealed coating evolution for hot forming steel. *IOP Conf. Ser. Mater. Sci. Eng.* **2018**, *292*, 012101. [CrossRef]
16. Sere, P.R.; Deya, C.; Elsner, C.I.; Di Sarli, A.R. Corrosion of painted galvanneal steel. *Procedia Mater. Sci.* **2015**, *8*, 1–10. [CrossRef]
17. Shojaee, M.; Midawi, A.R.H.; Barber, B.; Ghassemi-Armaki, H.; Worswick, M.; Biro, E. Mechanical properties and failure behavior of resistance spot welded third-generation advanced high strength steels. *J. Manuf. Process.* **2021**, *65*, 364–372. [CrossRef]
18. Ling, Z.; Chen, T.; Wang, M.; Kong, L. Reducing liquid metal embrittlement cracking in resistance spot welding of Q&P980 steel. *Mater. Manuf. Process.* **2020**, *35*, 1392–1399.
19. DiGiovanni, C.; Han, X.; Powell, A.; Biro, E.; Zhou, N.Y. Experimental and numerical analysis of liquid metal embrittlement crack location. *J. Mater. Eng. Perform.* **2019**, *28*, 2045–2052. [CrossRef]
20. DiGiovanni, C.; Shojaee, M.; Biro, E.; Zhou, N.Y. Effect of external loading on liquid metal embrittlement severity during resistance spot welding. *Manuf. Lett.* **2022**, *33*, 11–14. [CrossRef]
21. Yang, K.; Meschut, G.; Seitz, G.; Biegler, M.; Rethmeier, M. The identification of a new liquid metal embrittlement (LME) type in resistance spot welding of advanced high−strength steels on reduced flange widths. *Metals* **2023**, *13*, 1754. [CrossRef]
22. Beal, C.; Kleber, X.; Fabregue, D.; Bouzekri, M. Embrittlement of a zinc coated high manganese TWIP steel. *Mater. Sci. Eng. A-Struct. Mater. Prop. Microstruct. Process.* **2012**, *543*, 76–83. [CrossRef]
23. Siar, O.; Benlatreche, Y.; Dupuy, T.; Dancette, S.; Fabrègue, D. Effect of severe welding conditions on liquid metal embrittlement of a 3rd-generation advanced high-strength steel. *Metals* **2020**, *10*, 1166. [CrossRef]
24. Ghatei-Kalashami, A.; Ghassemali, E.; DiGiovanni, C.; Goodwin, F.; Zhou, N. Liquid metal embrittlement cracking behavior in iron-zinc (Fe/Zn) couple: Comparison of ferritic and austenitic microstructures. *Mater. Lett.* **2022**, *324*, 132780. [CrossRef]
25. Ma, H.; Gong, X.; Zhu, J.; Chen, H.; Li, J.; Liu, Y.; Ren, Q.; Zhang, F.; Pang, Z. Liquid metal embrittlement susceptibility of an oxide-dispersion strengthened FeCrAl alloy in contact with liquid lead-bismuth eutectic at 350 °C. *Corrosion Sci.* **2022**, *207*, 110603. [CrossRef]
26. Bhattacharya, D.; Cho, L.; van der Aa, E.; Pichler, A.; Pottore, N.; Ghassemi-Armaki, H.; Findley, K.O.; Speer, J.G. Influence of the starting microstructure of an advanced high strength steel on the characteristics of Zn-assisted liquid metal embrittlement. *Mater. Sci. Eng. A-Struct. Mater. Prop. Microstruct. Process.* **2021**, *804*, 140391. [CrossRef]
27. Akbari, E.; Kurnsteiner, P.; Steineder, K.; Gruber, M.; Arndt, M.; Letofsky-Papst, I.; Sierlinger, R.; Groiss, H. Insight into grain boundaries with reduced liquid metal embrittlement susceptibility in a boron-added 3rd generation advanced high strength steel. *Mater. Des.* **2024**, *237*, 112584. [CrossRef]
28. Wintjes, E.; DiGiovanni, C.; He, L.; Bag, S.; Goodwin, F.; Biro, E.; Zhou, Y. Effect of multiple pulse resistance spot welding schedules on liquid metal embrittlement severity. *J. Manuf. Sci. Eng.* **2019**, *141*, 101001. [CrossRef]
29. Ashiri, R.; Haque, M.A.; Ji, C.W.; Shamanian, M.; Salimijazi, H.R.; Park, Y.D. Supercritical area and critical nugget diameter for liquid metal embrittlement of Zn-coated twining induced plasticity steels. *Scr. Mater.* **2015**, *109*, 6–10. [CrossRef]
30. DiGiovanni, C.; Biro, E.; Zhou, N.Y. Impact of liquid metal embrittlement cracks on resistance spot weld static strength. *Sci. Technol. Weld. Join.* **2019**, *24*, 218–224. [CrossRef]
31. Tolf, E.; Hedegard, J.; Melander, A. Surface breaking cracks in resistance spot welds of dual phase steels with electrogalvanised and hot dip zinc coating. *Sci. Technol. Weld. Join.* **2013**, *18*, 25–31. [CrossRef]
32. El-Sari, B.; Biegler, M.; Rethmeier, M. Investigation of the LME susceptibility of dual phase steel with different zinc coatings. *Metals* **2023**, *13*, 890. [CrossRef]
33. Dong, W.; Pan, H.; Sun, Y.; Zhou, J.; Lei, M.; Ding, K.; Gao, Y. The sandwich-structured advanced high strength steel to resist the liquid metal embrittlement. *J. Mater. Res. Technol-JMRT* **2023**, *25*, 3167–3176. [CrossRef]
34. *ISO 5821*; Resistance Welding-Spot Welding Electrode Caps. ISO: Genève, Switzerland, 2009.
35. Aqra, F.; Ayyad, A. Surface tension (γLV), surface energy (γSV) and crystal-melt interfacial energy (γSL) of metals. *Curr. Appl Phys.* **2012**, *12*, 31–35. [CrossRef]
36. Zhou, J.; Sun, Y.; Wu, B.; Hu, T.; Lei, M.; Ding, K.; Gao, Y. Effect of the welding current on the liquid metal embrittlement in the resistance spot welded galvanized DP1180 advanced high strength steel. In *TMS 2024 153rd Annual Meeting & Exhibition Supplemental Proceedings*; Springer: Cham, Switzerland, 2024; pp. 923–930.
37. Dong, W.; Pan, H.; Lei, M.; Wang, S.; Ding, K.; Gao, Y. Three-dimension characterization of the liquid metal embrittlement crack in the resistance spot welded joint of the advanced high strength steel. *Mater. Today Commun.* **2023**, *34*, 105322. [CrossRef]

38. Kang, H.; Cho, L.; Lee, C.; De Cooman, B.C. Zn penetration in liquid metal embrittled TWIP steel. *Metall. Mater. Trans. A-Phys. Metall. Mater. Sci.* **2016**, *47*, 2885–2905. [CrossRef]
39. Ikeda, Y.; Yuan, R.; Chakraborty, A.; Ghassemi-Armaki, H.; Zuo, J.M.; Maaß, R. Early stages of liquid-metal embrittlement in an advanced high-strength steel. *Mater. Today Adv.* **2022**, *13*, 100196. [CrossRef]
40. Dong, W.; Pan, H.; Lei, M.; Ding, K.; Gao, Y. Zn penetration and its coupled interaction with the grain boundary during the resistance spot welding of the QP980 steel. *Scr. Mater.* **2022**, *218*, 114832. [CrossRef]
41. Lee, H.; Jo, M.C.; Sohn, S.S.; Kim, S.H.; Song, T.; Kim, S.K.; Kim, H.S.; Kim, N.J.; Lee, S. Microstructural evolution of liquid metal embrittlement in resistance-spot-welded galvanized twinning-induced plasticity (TWIP) steel sheets. *Mater. Charact.* **2019**, *147*, 233–241. [CrossRef]
42. Lalachan, A.; Murugan, S.P.; Jin, W.S.; Park, Y.D. Liquid metal embrittlement in Zn-coated steel resistance spot welding: Critical electrode-contact and nugget growth for stress development and cracking. *J. Mater. Process. Technol.* **2023**, *318*, 118009. [CrossRef]
43. Ghatei Kalashami, A.; Han, X.; Goodwin, F.; Zhou, N.Y. The influence of modified annealing during the galvanizing process on the resistance spot welding of the CMn1.8Si advanced high strength steel. *Surf. Coat. Technol.* **2020**, *381*, 125181. [CrossRef]
44. Vanden Eynde, X.; Servais, J.P.; Lamberigts, M. Investigation into the surface selective oxidation of dual-phase steels by XPS, SAM and SIMS. *Surf. Interface Anal.* **2003**, *35*, 1004–1014. [CrossRef]
45. Dong, W.; Lei, M.; Pan, H.; Ding, K.; Gao, Y. Role of the internal oxidation layer in the liquid metal embrittlement during the resistance spot welding of the Zn-coated advanced high strength steel. *J. Mater. Res. Technol-JMRT* **2022**, *21*, 3313–3326. [CrossRef]
46. Zhou, J.; Sun, Y.; Hu, T.; Pan, H.; Lei, M.; Ding, K.; Gao, Y. Uncovering the mechanism of the LME susceptibility for the galvanized and electrogalvanized DP 1180 steels. *Mater. Today Commun.* **2024**, *38*, 108530. [CrossRef]
47. Miyata, M.; Fushiwaki, Y.; Suzuki, Y.; Nagano, H.; Nagataki, Y. Effect of Si/Mn ratio on galvannealing behavior of Si-added steel. *ISIJ Int.* **2018**, *58*, 1600–1607. [CrossRef]

Disclaimer/Publisher's Note: The statements, opinions and data contained in all publications are solely those of the individual author(s) and contributor(s) and not of MDPI and/or the editor(s). MDPI and/or the editor(s) disclaim responsibility for any injury to people or property resulting from any ideas, methods, instructions or products referred to in the content.